JCI The Journal of Clinical Investigation

Astrocyte-derived VEGF-A drives blood-brain barrier disruption in CNS inflammatory disease

Azeb Tadesse Argaw, … , Michael V. Sofroniew, Gareth R. John

J Clin Invest. 2012;122(7):2454-2468. https://doi.org/10.1172/JCI60842.

Research Article **Neuroscience**

In inflammatory CNS conditions such as multiple sclerosis (MS), current options to treat clinical relapse are limited, and more selective agents are needed. Disruption of the blood-brain barrier (BBB) is an early feature of lesion formation that correlates with clinical exacerbation, leading to edema, excitotoxicity, and entry of serum proteins and inflammatory cells. Here, we identify astrocytic expression of VEGF-A as a key driver of BBB permeability in mice. Inactivation of astrocytic *Vegfa* expression reduced BBB breakdown, decreased lymphocyte infiltration and neuropathology in inflammatory and demyelinating lesions, and reduced paralysis in a mouse model of MS. Knockdown studies in CNS endothelium indicated activation of the downstream effector eNOS as the principal mechanism underlying the effects of VEGF-A on the BBB. Systemic administration of the selective eNOS inhibitor cavtratin in mice abrogated VEGF-A–induced BBB disruption and pathology and protected against neurologic deficit in the MS model system. Collectively, these data identify blockade of VEGF-A signaling as a protective strategy to treat inflammatory CNS disease.

Astrocyte-derived VEGF-A drives blood-brain barrier disruption in CNS inflammatory disease

Azeb Tadesse Argaw,[1,2,3] Linnea Asp,[1,2,3] Jingya Zhang,[1,2,3] Kristina Navrazhina,[1,2,3] Trinh Pham,[1,2,3] John N. Mariani,[1,2,3] Sean Mahase,[1,2,3] Dipankar J. Dutta,[1,2,3] Jeremy Seto,[1,2,3] Elisabeth G. Kramer,[1,2,3] Napoleone Ferrara,[4] Michael V. Sofroniew,[5] and Gareth R. John[1,2,3]

[1]Corinne Goldsmith Dickinson Center for MS, [2]Friedman Brain Institute, and [3]Department of Neurology, Mount Sinai School of Medicine (MSSM), New York, New York, USA. [4]Genentech, South San Francisco, California, USA. [5]Department of Neurobiology, David Geffen School of Medicine, UCLA, Los Angeles, California, USA.

In inflammatory CNS conditions such as multiple sclerosis (MS), current options to treat clinical relapse are limited, and more selective agents are needed. Disruption of the blood-brain barrier (BBB) is an early feature of lesion formation that correlates with clinical exacerbation, leading to edema, excitotoxicity, and entry of serum proteins and inflammatory cells. Here, we identify astrocytic expression of VEGF-A as a key driver of BBB permeability in mice. Inactivation of astrocytic *Vegfa* expression reduced BBB breakdown, decreased lymphocyte infiltration and neuropathology in inflammatory and demyelinating lesions, and reduced paralysis in a mouse model of MS. Knockdown studies in CNS endothelium indicated activation of the downstream effector eNOS as the principal mechanism underlying the effects of VEGF-A on the BBB. Systemic administration of the selective eNOS inhibitor cavtratin in mice abrogated VEGF-A–induced BBB disruption and pathology and protected against neurologic deficit in the MS model system. Collectively, these data identify blockade of VEGF-A signaling as a protective strategy to treat inflammatory CNS disease.

Introduction

The blood-brain barrier (BBB) acts as a selective interface insulating the CNS parenchyma from the circulation (1). It exists at the level of microvascular endothelial cells (MVECs), which restrict permeability using complex tight junctions (2). Claudins — including CLN-3, CLN-5, and CLN-12 — play key roles in junction formation at the BBB, which fails to seal in *Cln5*$^{-/-}$ mice (3, 4), whereas occludin (OCLN) regulates junction properties (5). Establishment, maintenance, and repair of the endothelial barrier depend on pericytes (6–8) and astrocytes (9–11), and both are also linked to BBB disruption in disease (8, 12).

BBB permeability is an early and prominent feature of inflammatory CNS conditions, including MS (13), viral encephalitis (14), and traumatic and hypoxic/ischemic injury (15). BBB disruption correlates with neurologic exacerbation, and MS patients with contrast-enhancing plaques are more likely to have irreversible pathology (13, 16). BBB breakdown leads to edema, metabolic imbalance, excitotoxicity, and ingress of factors that potentiate inflammation and inhibit repair (17–20) and facilitates infiltration of T and B lymphocytes, macrophages, and neutrophils (21). In diseases such as MS, current options to restrict relapse severity are limited, and patients may benefit from more selective agents (22).

Recently, we identified a link between reactive astrocytes and BBB breakdown (12, 23). Analyses of human cultures revealed that inflammatory cytokines implicated in lesion pathogenesis induce astrocytic expression of angiogenic factors, including VEGF-A and its regulator, HIF-1α (23). VEGF-A is a primary driver of vessel formation, and even heterozygous mutants display vascular abnormalities and embryonic lethality (24, 25). In inflammatory CNS disorders including MS, VEGF-A is reexpressed by reactive astrocytes and signals in CNS endothelium via VEGFR2 (26, 27). VEGF-A disrupts CLN-5 and OCLN expression in CNS endothelial cultures and induces BBB breakdown and immune cell infiltration in vivo (12, 27).

Here, using mice with VEGF-A inactivation targeted to reactive astrocytes (*GfapCre:Vegfa*$^{fl/fl}$ mice), we identified astrocyte-derived VEGF-A as an important driver of BBB permeability, lymphocyte infiltration, tissue damage, and clinical deficit. Moreover, we showed that these effects were mediated via activation of the downstream effector eNOS. Collectively, our findings identified blockade of VEGF-A signaling as a protective avenue in inflammatory CNS disorders. Since this approach targets events within the endothelial cell, it allows for systemic treatment administration, bypassing the need for delivery into the parenchyma.

Results

GfapCre:Vegfa$^{fl/fl}$ *mice show normal postnatal survival.* To inactivate VEGF-A in reactive astrocytes in vivo, we bred *mGfapCre* mice (28) with animals containing a floxed *Vegfa* allele (29), both on the C57BL/6 background (Figure 1, A and B). Experimental *GfapCre:Vegfa*$^{fl/fl}$ pups represented one-quarter of offspring from final matings and survived normally to adulthood. CNS vascular patterns and expression of the BBB tight junction components CLN-5 and OCLN were normal in *GfapCre:Vegfa*$^{fl/fl}$ adults (Figure 1, C and D), and no parenchymal leakage of serum fibrinogen, albumin, or Ig was detected (Figure 1C). Extravasation of these proteins has been widely used as a marker of BBB opening (8, 11, 17).

Efficient VEGF-A inactivation of the inflamed CNS in GfapCre:Vegfa$^{fl/fl}$ *mice.* In human astrocytes, VEGF-A was expressed strongly in response to the cytokine IL-1β (Figure 1E), an important early contributor to inflammatory lesion pathogenesis. To validate inactivation of astrocytic *Vegfa* in *GfapCre:Vegfa*$^{fl/fl}$ mice, we used

Conflict of interest: The authors have declared that no conflict of interest exists.
Citation for this article: *J Clin Invest.* 2012;122(7):2454–2468. doi:10.1172/JCI60842.

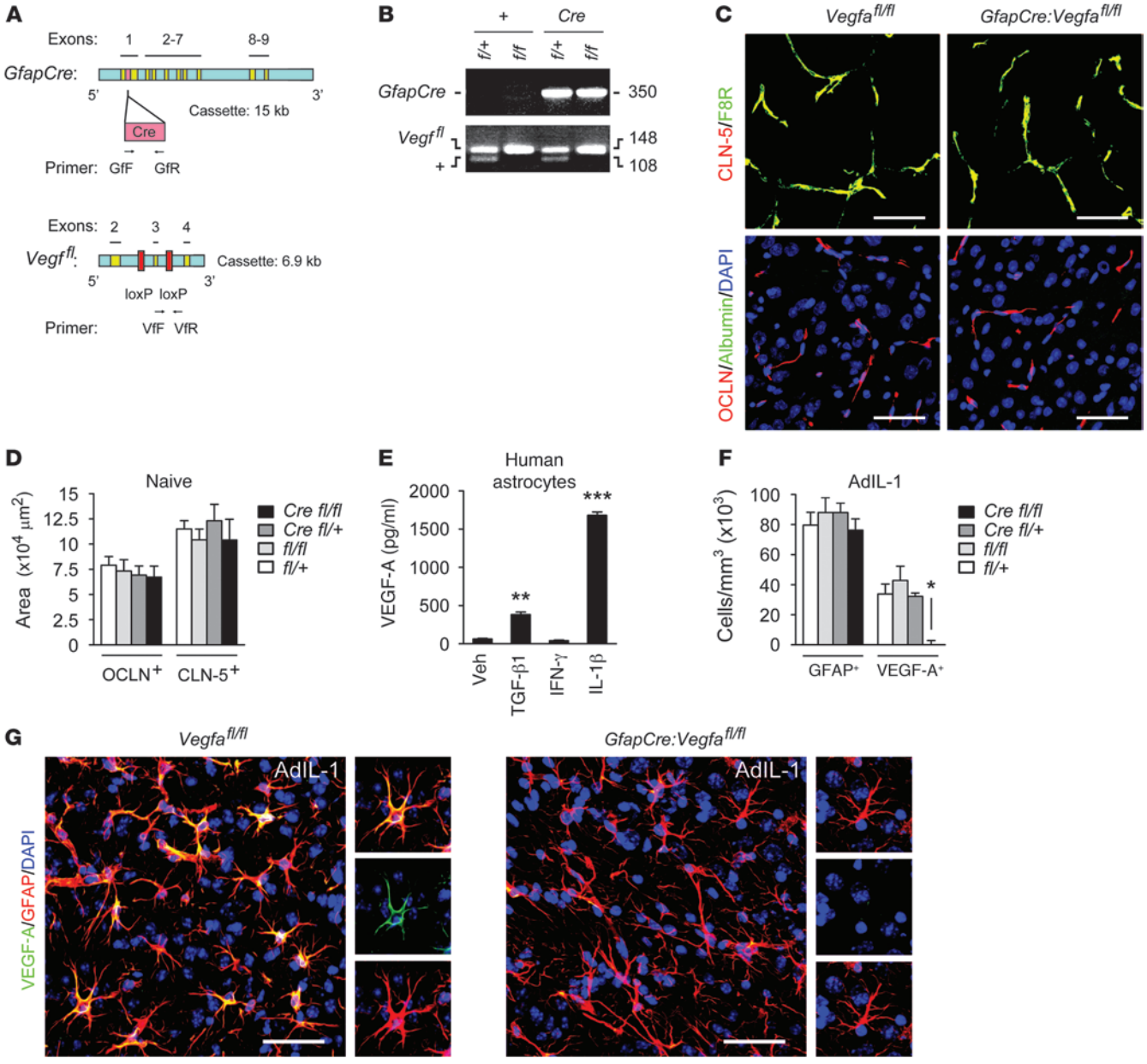

Figure 1

Efficient inactivation of VEGF-A in the inflamed CNS in *GfapCre:Vegfa*$^{fl/fl}$ mice. (**A**) Mice with loxP sites flanking *Vegfa* exon 3 were bred with an *mGfapCre* line. (**B**) Final matings generated *GfapCre:Vegfa*$^{fl/fl}$ mice and *GfapCre:Vegfa*$^{+/fl}$, *Vegfa*$^{fl/fl}$, and *Vegfa*$^{+/fl}$ controls, with experimental pups representing 25% of total. (**C** and **D**) Immunoreactivity for the endothelial protein F8R and BBB junction components CLN-5 and OCLN in cerebral cortices of 12-week-old *GfapCre:Vegfa*$^{fl/fl}$ mice and littermates (n = 3 per genotype). (**E**) ELISA of primary human astrocytes showing VEGF-A induction by vehicle or 10 ng/ml IL-1β, TGF-β1, or IFN-γ at 24 hours. Results are typical of cultures from 3 separate brains. (**F** and **G**) AdIL-1 (10^7 pfu) was microinjected into cortical gray matter of 12-week-old *GfapCre:Vegfa*$^{fl/fl}$ mice and littermates (n = 21, at least 4 per genotype); animals were sacrificed at 7 dpi, based on time course studies (see Supplemental Figures 1 and 2); and lesions were stained and examined to determine the number of GFAP$^+$ and VEGF-A$^+$ cells. Data are representative of 3 independent experiments. In **G**, individual channels from sections of the merged images are shown at right. See Supplemental Figure 1D for higher-magnification images of VEGF-A$^+$GFAP$^+$ cells. Scale bars: 50 μm (**C** and **G**). $^*P < 0.05$, $^{**}P < 0.01$, $^{***}P < 0.001$, ANOVA plus Bonferroni test.

microinjection of an IL-1β vector, AdIL-1 (30, 31), into cortical gray matter. In uninjected or empty vector–injected cortices of 12-week-old mice, GFAP immunoreactivity was low in all genotypes, and VEGF-A was not detected (Supplemental Figure 1, A and B; supplemental material available online with this article; doi:10.1172/JCI60842DS1). Conversely, AdIL-1–injected cortices exhibited hypercellular lesions containing GFAP$^+$ reactive astrocytes, with numbers maximal at 7 days postinduction (dpi) (Supplemental Figure 1, A and B). In controls at 7 dpi, lesions were also positive for VEGF-A, which localized to GFAP$^+$ cells (Figure 1,

F and G, and Supplemental Figure 1, A–D). However, almost no VEGF-A$^+$ cells were seen in lesions in *GfapCre:Vegfa$^{fl/fl}$* animals (Figure 1, F and G). Thus, VEGF-A expression in inflammatory CNS plaques was astrocyte specific, and recombination-mediated inactivation was efficient in *GfapCre:Vegfa$^{fl/fl}$* mice.

Reduced BBB breakdown in GfapCre:Vegfa$^{fl/fl}$ mice. Confocal projections from cortices of 12-week-old mice revealed intimate association of GFAP$^+$ astrocytic endfeet with CLN-5$^+$ and OCLN$^+$ endothelium (Figure 2A). VEGFR2 localized to endothelial cells within the CNS (Figure 2B) and to the cell membrane of mouse cortical or spinal cord MVECs in vitro (Supplemental Figure 2A). In both cultures, VEGF-A (10 ng/ml) selectively downregulated CLN-5 and OCLN (Figure 2, C–E). CLN-5 and OCLN expression were also disrupted in VEGF-A–treated human MVECs at 16 hours and undetectable at 24 and 48 hours, but neither responded to other factors tested (Supplemental Figure 2, B and C).

Microinjection of AdIL-1 into cortical gray matter resulted in disruption of CLN-5 and OCLN as well as BBB breakdown at 7 dpi in controls (Supplemental Figure 2, D and E, and Figure 2, F–I), correlating with astrocytic VEGF-A expression (compare with Supplemental Figure 1, A–C, and Figure 1, F and G). However, in *GfapCre:Vegfa$^{fl/fl}$* mice, CLN-5 and OCLN immunoreactivity was rescued and linear staining profiles typical of uninjected CNS were retained (Figure 2, F–H), and parenchymal leakage of serum proteins was minimal (Figure 2, F, G, and I). Thus, inactivation of astrocytic VEGF-A resulted in preservation of BBB components and inhibition of BBB breakdown in inflammatory lesions.

Reduced lymphocyte infiltration in GfapCre:Vegfa$^{fl/fl}$ mouse lesions. AdIL-1 lesions in control genotypes contained activated CD11b$^+$ microglia (Figure 3, A and B), CD4$^+$ T lymphocytes (Figure 3, B and C), and small numbers of CD19$^+$ B cells (Figure 3C). Inflammation paralleled BBB disruption and was maximal at 7 dpi. However, T cell numbers were reduced in lesions in *GfapCre:Vegfa$^{fl/fl}$* mice (Figure 3, B and C), and no CD19$^+$ cells were detected, compared with 1,554 ± 294 cells/mm^3 in *Vegfa$^{fl/fl}$* controls. Numbers of CD11b$^+$ cells and GFAP$^+$ reactive astrocytes were unchanged (Figure 3, A and B, and Figure 1F).

We reasoned that BBB integrity might directly limit lymphocyte entry into the CNS in *GfapCre:Vegfa$^{fl/fl}$* mice. Alternatively, peripheral lymphocytes might be reduced, or CNS expression of adhesion molecules, chemokines, or MMPs might be restricted. However, we found that peripheral lymphocyte numbers were normal in naive *GfapCre:Vegfa$^{fl/fl}$* animals, and numbers of T and B cells in peripheral lymphoid organs were identical to those of other genotypes (Supplemental Figure 3, A–D). Moreover, AdIL-1 lesions in *GfapCre:Vegfa$^{fl/fl}$* animals displayed normal endothelial immunoreactivity for VCAM-1, ICAM-1, CXCL10, and CXCL12 (Figure 3, D and E) and normal CNS induction of MMP-9 and MMP-3 (Figure 3, F and G). In addition, in CNS MVEC cultures, IL-1β strongly induced VCAM-1, ICAM-1, CXCL1, CXCL8, CXCL10, and CCL2 and the cytokines IL-6 and TNF-α, but none of these factors was VEGF-A responsive (Figure 3, H and I).

We compared these results with data from animals receiving therapies currently used in MS patients in relapse, for example, 50 mg/ml methylprednisolone (MP) (32). In mice receiving MP prior to AdIL-1, BBB breakdown, lymphocyte infiltration, and VEGF-A immunoreactivity were restricted (Figure 3, J and K). However, these effects were part of a more extensive cohort of changes, including reduced numbers of reactive astrocytes (Figure 3J) and inhibition of endothelial adhesion molecule expression (Figure 3K).

These results showed that lymphocyte infiltration into AdIL-1–induced inflammatory lesions was restricted in *GfapCre:Vegfa$^{fl/fl}$* mice, which correlated with reduced BBB disruption, but was not associated with wider immune suppression, such as was seen in steroid-treated animals. These data were compatible with previous work showing that BBB breakdown facilitates lymphocyte entry into the CNS parenchyma (21).

Reduced neuropathology in focal gray and white matter lesions in GfapCre:Vegfa$^{fl/fl}$ mice. We examined changes in neuropathology in *GfapCre:Vegfa$^{fl/fl}$* mice (Figure 4 and Supplemental Figure 4). The number and organization of cortical NeuN$^+$ neurons was normal in unchallenged *GfapCre:Vegfa$^{fl/fl}$* adults, and no neuronal apoptosis was observed (Supplemental Figure 4A). In controls, we observed areas of neuronal loss in cortical AdIL-1 lesions at 7 dpi, in areas of inflammation and BBB disruption (Figure 4, A–C). Apoptotic cleaved caspase-3$^+$NeuN$^+$ neurons were present at the borders of these areas (Figure 4, D and E). Both parameters were reduced in lesions of *GfapCre:Vegfa$^{fl/fl}$* mice (Figure 4, A, B, D, and E). Plotting neuronal loss against BBB breakdown for individual mice showed that each was smallest in *GfapCre:Vegfa$^{fl/fl}$* animals (Figure 4C).

White matter pathology was also reduced in focal demyelinating lesions in *GfapCre:Vegfa$^{fl/fl}$* mice. Immunoreactivity for myelin basic protein (MBP) and numbers of Olig2$^+$ oligodendrocytes were normal in naive *GfapCre:Vegfa$^{fl/fl}$* adults (Supplemental Figure 4, B–D). Microinjection of lysolecithin into the corpus callosum resulted in focal demyelination (Figure 4, F and G), which was maximal at 7 dpi and accompanied by BBB disruption and accumulation of T and B lymphocytes, GFAP$^+$ reactive astrocytes, and CD11b$^+$ microglia (ref. 33 and data not shown). However, the cross-sectional demyelinated area in *GfapCre:Vegfa$^{fl/fl}$* mice was smaller than in controls (Figure 4, F and G), and oligodendrocyte loss was less pronounced (Figure 4, H and I).

Diminished EAE clinical deficit and tissue damage in GfapCre:Vegfa$^{fl/fl}$ mice. To examine the relevance of these findings to disease, we investigated the phenotype of EAE, a model of MS, in *GfapCre:Vegfa$^{fl/fl}$* mice (Figure 5 and Supplemental Figure 5). Compatible with previous EAE studies in conditional mutant lines (34), we crossed the experimental genotype with non-*Cre* homozygotes to generate *GfapCre:Vegfa$^{fl/fl}$* mice and *Vegfa$^{fl/fl}$* controls at a 50:50 ratio in the numbers required for this work.

Mice (8-week-old males, at least 10 per group) were sensitized with encephalitogenic myelin oligodendrocyte glycoprotein 35–55 in CFA ($MOG_{35–55}$/CFA), and clinical deficit was evaluated using a 5-point paradigm (35). Ascending paralysis was observed from 7 dpi, and the deficit increased in *Vegfa$^{fl/fl}$* controls until 19 days, when clinical score stabilized at a mean of 2.84, representing severe hindlimb weakness approaching complete paralysis (Figure 5A). *GfapCre:Vegfa$^{fl/fl}$* mice showed much milder signs, which reached a plateau at 16 days at a mean of 1.21, indicative of a limp tail. The divergence in scores reached significance at 13, 14, and 17–21 dpi (i.e., through the end of the experiment; Figure 5A). Examination of peak severity in each mouse showed that 53% of controls, compared with 1 *GfapCre:Vegfa$^{fl/fl}$* mouse (10%), displayed complete hindlimb paralysis or worse during the study (score ≥ 3) (Figure 5B). Mortality or severe paralysis requiring euthanasia (score ≥ 4) occurred in 33% of controls compared with 0 *GfapCre:Vegfa$^{fl/fl}$* mice (Figure 5B).

The reduction of clinical disease in *GfapCre:Vegfa$^{fl/fl}$* mice was associated with decreased tissue damage (Figure 5, C–K). In spinal cords of controls at 21 dpi, typical pathology of EAE was observed, including astrogliosis (Figure 5C), BBB breakdown

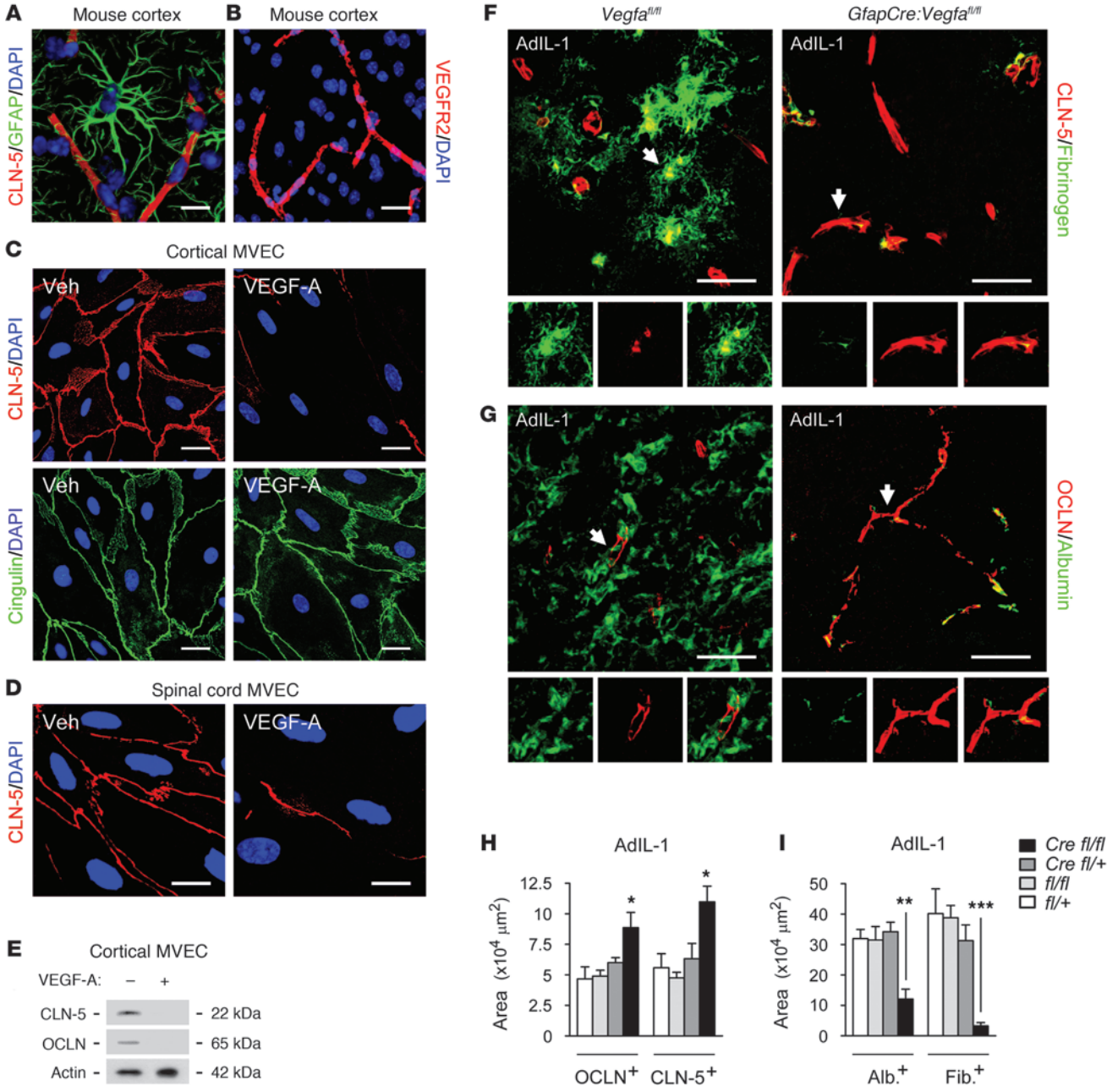

Figure 2

GfapCre:Vegfa$^{fl/fl}$ animals display reduced BBB breakdown. (**A**) 3-dimensionally rendered projection from cortex of a 12-week-old C57BL/6 mouse, illustrating intimate association of GFAP$^+$ astrocytic endfeet with CLN-5$^+$ endothelium. (**B**) Cortical section from the same mouse immunostained for VEGFR2, demonstrating localization to endothelium. (**C**–**E**) MVEC cultures from mouse cortex (**C** and **E**) and spinal cord (**D**) were treated with vehicle or 10 ng/ml VEGF-A and harvested at 24 hours, followed by immunostaining (**C** and **D**) and immunoblotting (**E**). Results are typical of data from 3 separate cultures. (**F**–**I**) AdIL-1–injected cerebral cortices from 12-week-old *GfapCre:Vegfa*$^{fl/fl}$ mice and littermates sacrificed at 7 dpi (n = 21, at least 4 per genotype, as in Figure 1). (**F** and **G**) Immunostaining for CLN-5 (**F**) and OCLN (**G**). Individual channels from sections of the merged images are shown below, enlarged 1.5-fold. (**H**) Morphometry of OCLN and CLN-5. (**I**) Morphometry of albumin and fibrinogen extravasation (measures of BBB breakdown). Data are representative of 3 independent experiments. Scale bars: 20 μm (**A** and **C**); 40 μm (**B**); 10 μm (**D**); 50 μm (**F** and **G**). $^*P < 0.05$, $^{**}P < 0.01$, $^{***}P < 0.001$, ANOVA plus Bonferroni test.

(Figure 5D), inflammatory cell infiltration (Figure 5E), and multifocal demyelination and oligodendrocyte loss (Figure 5F). VEGF-A was strongly expressed in lesions in controls, localizing to GFAP$^+$ reactive astrocytes, but VEGF-A$^+$ cells were almost completely absent from plaques in *GfapCre:Vegfa*$^{fl/fl}$ mice (Figure 5, C and G). Numbers of reactive astrocytes were also reduced (Figure 5, C and G). CLN-5 expression was largely maintained in lesions in *GfapCre:Vegfa*$^{fl/fl}$ animals (Figure 5, D and H), and BBB break-

down was restricted (Figure 5, D and I). Infiltration of $CD45^+$ inflammatory cells was diminished (Figure 5, E and J). Importantly, these changes were associated with reduced demyelination and with oligodendrocyte preservation (Figure 5, F and K). No differences in lymphocyte numbers were seen in peripheral lymphoid organs of *GfapCre:Vegfa$^{fl/fl}$* mice versus controls with EAE (Supplemental Figure 5, A–D).

Collectively, these results revealed that inhibition of BBB disruption in *GfapCre:Vegfa$^{fl/fl}$* mice was associated with reduced pathology in focal gray and white matter lesions (Figure 4) and with restriction of paralysis and mortality in a model of MS (Figure 5). They identified attenuation of VEGF-A signaling as an avenue for protective intervention in inflammatory CNS disease.

No inhibition of VEGF-A expression or rescue of BBB disruption in GfapCre:Hif1a$^{fl/fl}$ mice. As a translational approach, we initially investigated inhibition of astrocytic VEGF-A production by targeting the transcription factor HIF-1α, a developmental regulator of VEGF-A that is reexpressed by reactive astrocytes in conditions including MS (refs. 23, 36, and Figure 6). Compatible with previous reports (23), HIF-1α was expressed in human astrocyte cultures in response to IL-1β, with maximal expression at 24 hours (Figure 6A), and localized to astrocytic nuclei (Figure 6B), consistent with functionality. To inactivate *Hif1a* selectively in vivo, we crossed *mGfapCre* mice with a floxed *Hif1a* allele (37). Final breedings produced *GfapCre:Hif1a$^{fl/fl}$* mice at a frequency of 25%, and pups were healthy, with normal CNS CLN-5 and OCLN immunoreactivity and an intact BBB (data not shown).

In adults, HIF-1α was not observed in naive cortices, but was strongly expressed in AdIL-1–induced lesions in controls at 7 dpi, where it localized to nuclei of $GFAP^+$ reactive astrocytes (Figure 6, C and D). In contrast, $HIF\text{-}1\alpha^+$ cells were almost absent in lesions in *GfapCre:Hif1a$^{fl/fl}$* mice (Figure 6, C and D). However, inactivation of *Hif1a* did not reduce astrocytic VEGF-A immunoreactivity in inflammatory lesions (Figure 6, C and E), and disruption of CLN-5 and BBB breakdown were unmitigated (Figure 6, F and G). Thus, selective inactivation of *Hif1a* was ineffective in inhibiting astrocytic VEGF-A expression and BBB disruption in inflammatory lesions.

VEGF-A downregulates CLN-5 expression via the VEGFR2 receptor. As an alternate strategy, we examined mechanisms underlying VEGF-A effects in CNS endothelium (Figures 7 and 8 and Supplemental Figure 6). Immunoblotting for receptors in human CNS MVEC cultures detected VEGFR1 and VEGFR2 and the coreceptor NRP1, but not NRP2 (data not shown). Antibody blockade of VEGFR2 abrogated VEGF-A downregulation of CLN-5 and OCLN in CNS MVECs (Figure 7, A and B). NRP1 played a minor role in these events: $VEGF_{121}$ (a ligand for VEGFR2, but not NRP1; ref. 38) had mildly weaker effects on CLN-5 than $VEGF_{165}$ (which binds to both) (Supplemental Figure 6A). Activation of VEGFR1 using its selective agonist, P*l*GF, or antibody blockade did not affect CLN-5 or OCLN (data not shown).

To confirm the relevance of VEGFR2 signaling in vivo, we coinjected 20 ng VEGF-A or vehicle with either VEGFR2-blocking antibody or IgG control (2 μg) into cortices of 12-week-old C57BL/6 mice ($n = 3$ per group). Animals were sacrificed at 24 hours. VEGF-A caused disruption of endothelial CLN-5 and OCLN and BBB breakdown, but VEGFR2 blockade inhibited these events (Figure 7, C and D). Thus, the effects of VEGF-A on BBB junction components were VEGFR2 dependent.

Effects of VEGF-A on CLN-5 are mediated via eNOS. Treatments to inhibit astrocytic VEGF-A production or binding to endothelial VEGFR2 would require entry to the CNS parenchyma, across the BBB. In contrast, agents targeting VEGF-A signaling in CNS endothelium could enter the cell from the circulation via the luminal surface, and so could be delivered systemically. We therefore analyzed signaling pathways underlying the effects of VEGF-A in CNS endothelial cells.

VEGFR2 activates 4 pathways in endothelium (Figure 7A): PLCγ, which stimulates MEK-MAPK; Shb activation of PI3K-Akt; TSAd and Src; and p38 (39). Additionally, VEGF-A activates eNOS via PLCγ and PI3K. In human CNS MVECs, VEGF-A induced phosphorylation of the PI3K pathway transcription factor GSK3 (S21/9), MEK kinase p44/42 (T202/Y204), and Src (Y416). Responses of GSK3 and p44/42 peaked at 16 hours, whereas strong Src phosphorylation was seen at both 6 and 16 hours (Supplemental Figure 6, B and C). VEGF-A also induced phosphorylation of eNOS (S1177), which increased progressively to 24 hours (Supplemental Figure 6, B and C). No activation of p38 (T180/Y182) was observed.

In pharmacologic studies, PLCγ1 blockade using 5 μM U73122 inhibited VEGF-A downregulation of CLN-5, whereas inhibition of Src kinase, p44/42, or PI3K had no effect (Figure 7E). These findings implicated PLCγ, but showed that it was not acting via MAPKs, and so we focused on eNOS, the other PLCγ effector in VEGF-A signaling. To inhibit eNOS in CNS MVEC cultures, we initially used cavtratin, a cell-permeable fusion protein that selectively blocks eNOS enzymatic activity via protein-protein interaction without affecting other forms of NOS (40–42). Importantly, VEGF-A disruption of CLN-5 was abrogated by pretreatment with 2 μM cavtratin (Figure 7F). VEGF-A downregulation of CLN-5 in human CNS MVECs was also specifically inhibited by siRNA silencing of eNOS expression (Figure 7G). Interestingly, higher concentrations of other NOS inhibitors, including 100 μM L-N5-(1-iminoethyl) ornithine,dihydrochloride (L-NIO) (43), gave similar results in endothelial cells (Supplemental Figure 6D). To test inhibitor specificity, we examined the effects on iNOS expression and NO release in LPS-stimulated macrophages or astrocytes treated with IL-1β plus IFN-γ. Compatible with previous findings (40), and in contrast to its marked effects in endothelial cells, cavtratin had no effect on NO production in these systems, whereas all other inhibitors tested significantly reduced nitrite levels (Supplemental Figure 6E). Collectively, these data suggest cavtratin inhibition of endothelial VEGF-A signaling as a potential therapeutic avenue by which to inhibit BBB breakdown in vivo.

Peripherally delivered cavtratin abrogates VEGF-induced BBB disruption and pathology. Within the adult CNS, eNOS immunoreactivity localized to endothelial cells (Supplemental Figure 6F). To test the effect of eNOS blockade on the effects of VEGF-A in vivo, we administered 2.5 mg/kg cavtratin or vehicle i.p. to 12-week-old C57BL/6 mice (3 per group), then 30 minutes later microinjected 60 ng VEGF-A or control into cortical layers IV and V (Figure 7, H–K). Cavtratin abrogated VEGF-A–induced disruption of endothelial CLN-5 and OCLN and BBB breakdown at 24 hours and prevented lymphocyte infiltration and neuronal loss (Figure 7, H–K).

Similar effects were observed in AdIL-1–induced lesions (Figure 7, L and M). Mice received 2.5 mg/kg cavtratin or vehicle 30 minutes prior to cortical microinjection of AdIL-1, then daily for 7 days. In animals receiving cavtratin, endothelial CLN-5 was rescued in AdIL-1–injected cortices, and BBB disruption was inhibited (Figure 7, L and M). Endothelial eNOS expression was increased in AdIL-1 lesions, compatible with previous reports (44). Consistent with its posttranslational mechanism, cavtratin did not alter eNOS immunoreactivity (Supplemental Figure 6, G and H).

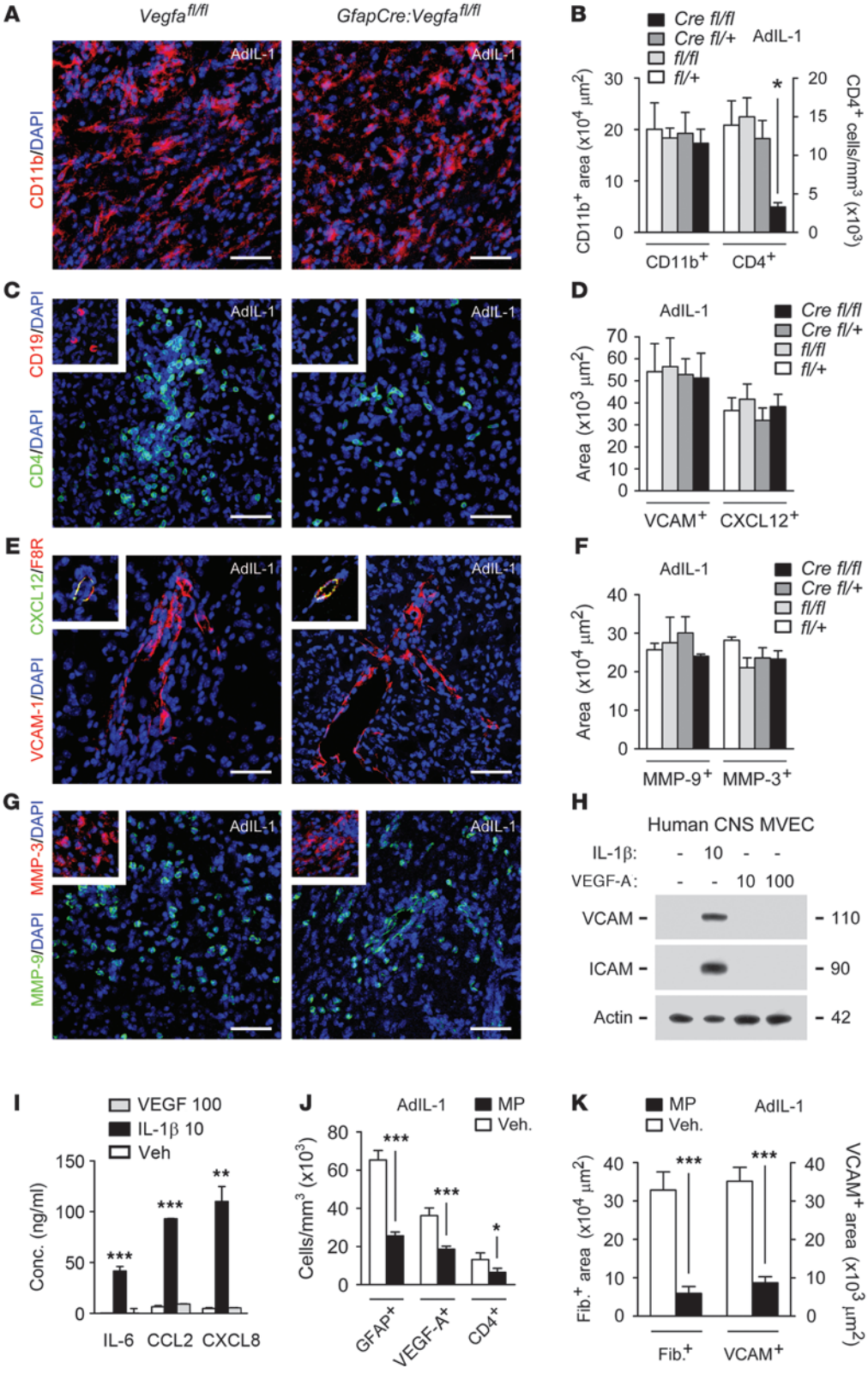

Figure 3

Reduced lymphocyte infiltration in *GfapCre:Vegfa*$^{fl/fl}$ mice. (**A**–**G**) AdIL-1–microinjected cortices were harvested at 7 dpi from 12-week-old *GfapCre:Vegfa*$^{fl/fl}$ mice and littermates (at least 4 per genotype, $n = 21$). Shown are immunostaining and morphometry of (**A** and **B**) CD11b, (**B** and **C**) CD4, (**C**) CD19, (**D** and **E**) VCAM-1 and CXCL12, and (**F** and **G**) MMP-9 and MMP-3. Data are representative of findings from 3 independent experiments. (**H** and **I**) Human CNS MVECs were treated with 10 ng/ml IL-1β or 10 or 100 ng/ml VEGF-A for 24 hours, and (**H**) expression of VCAM-1 and ICAM-1 were determined by immunoblotting, and (**I**) concentrations of CC and CXC chemokines and cytokines were quantified. Data are representative of 3 experiments in separate cultures. (**J** and **K**) 12-week-old C57BL/6 mice ($n = 4$ per group) received 50 mg/ml MP or vehicle i.p., then intracerebral microinjection of AdIL-1 24 hours later, and were sacrificed at 7 dpi and examined to determine (**J**) the proportion of GFAP$^+$, VEGF-A$^+$, and CD4$^+$ cells (measures of immunoreactivity and lymphocyte infiltration) and (**K**) the expression of fibrinogen and VCAM (measures of BBB breakdown). Data are representative of findings from 3 independent experiments. Scale bars: 50 µm (**A**, **C**, **E**, **G**, and all insets). $^*P < 0.05$, $^{**}P < 0.01$, $^{***}P < 0.001$, ANOVA plus Bonferroni test (**B**, **D**, **F**, and **I**) or Student's *t* test (**J** and **K**).

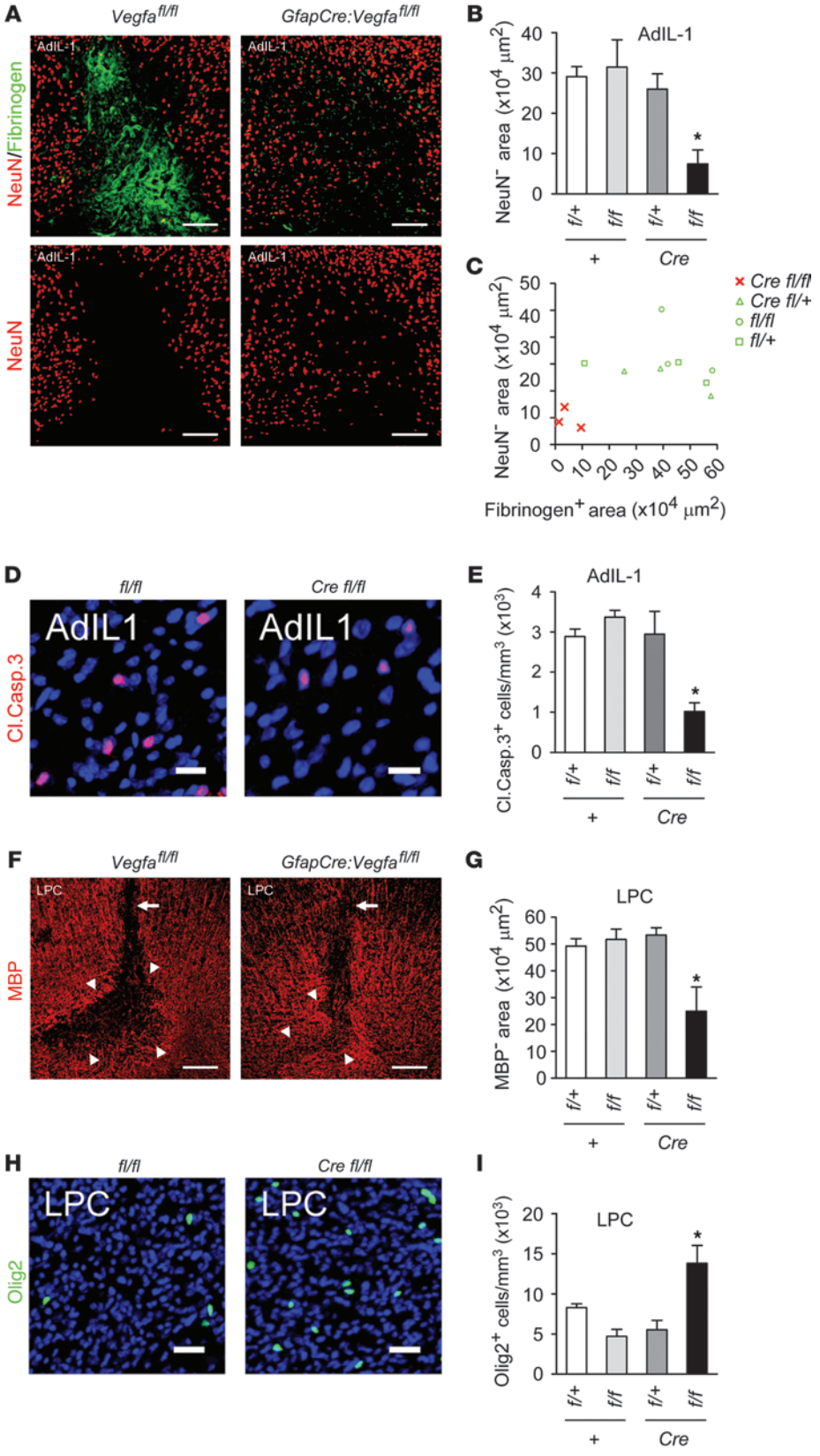

Figure 4

Reduced neuropathology in *GfapCre:Vegfa*$^{fl/fl}$ animals. (**A**–**C**) AdIL-1–injected cortices from 12-week-old *GfapCre:Vegfa*$^{fl/fl}$ mice and littermates (7 dpi, n = 3 per genotype) were (**A**) stained for NeuN (also shown separately) and fibrinogen, and neuronal loss was quantified and plotted (**B**) per group and (**C**) against fibrinogen area (a measure of BBB breakdown). (**D** and **E**) Cells from **A**–**C** were (**D**) stained for cleaved caspase-3, and (**E**) the proportion of cleaved caspase-3–positive cells was determined (a measure of apoptosis). (**F**–**I**) *GfapCre:Vegfa*$^{fl/fl}$ mice and littermates (12 weeks old, n = 3 per genotype) received a stereotactic microinjection of lysolecithin into the corpus callosum and sacrificed at 7 dpi. (**F** and **G**) Immunostaining and quantification for MBP (a measure of demyelination). Arrowheads, extent of demyelination; arrows, injection tracks. (**H** and **I**) Staining and morphometry for Olig2 (a marker of oligodendrocyte loss). Scale bars: 150 μm (**A** and **F**); 15 μm (**D** and **H**). *P < 0.05, ANOVA plus Bonferroni test. Results are representative of data from 3 independent studies.

Cavtratin protects against paralysis in EAE. We tested the effect of cavtratin administration on clinical disease and CNS damage in EAE, comparing the results with the phenotype seen in *GfapCre:Vegfa*$^{fl/fl}$ mice (Figure 8, compare with Figure 5). Mice (8-week-old male C57BL/6, 10 per group) were sensitized with $MOG_{35–55}$/CFA (35), then treated daily for 7 days from the onset of weight loss (>10% BW) with 2.5 mg/kg/d cavtratin or vehicle i.p., and neurological signs were evaluated as described previously (35).

Weight loss occurred — and therapy was concurrently initiated — at 7 dpi, and ascending paralysis was first observed 24 hours later, with severity in controls increasing until 16 days, when neurologic deficit reached a plateau at a mean of 3.22, indicative of complete hindlimb paralysis plus mild forelimb weakness (Figure 8A). Signs in cavtratin-treated mice were much less severe, and peaked at 17 days at a mean of 1.78 (limp tail with mild hindlimb weakness). The difference in scores was significant at 12–16 days (Figure 8A). Comparison of peak clinical severity in each animal was even more revealing: almost all controls (90%), but less than half of cavtratin-treated mice (40%), displayed complete hindlimb paralysis or worse (score ≥ 3) (Figure 8B). In controls, mortality or severe paralysis requiring euthanasia (score ≥ 4) was 40%, compared with 10% in the cavtratin-treated group (Figure 8B). Neuropathology was also decreased in cavtratin-treated mice (Figure 8, C–F). CLN-5 immunoreactivity was rescued and BBB disruption and inflammatory cell infiltration inhibited (Figure 8, C–E), and myelin and oligodendrocytes were preserved (Figure 8, C and F).

These findings were compatible with our EAE data from *GfapCre:Vegfa*$^{fl/fl}$ mice and showed that cavtratin treatment during the acute clinical phase of a model of MS protected against paralysis and neuropathology. Our results therefore suggested blockade of endothelial VEGF-A signaling as an avenue by which to restrict neurological deficit and tissue damage.

Discussion

In this study, we defined a therapeutic approach for inflammatory CNS disease using inhibition of BBB breakdown to restrict clinical severity and permanent pathology, which we believe to be novel. This approach is based on our identification of a mechanism whereby reactive astrocytes mediate disruption of BBB integrity (Figure 9). Our findings showed that the angiogenic factor VEGF-A was an important effector used by reactive astrocytes to drive vascular permeability and CNS damage in acute inflammatory lesions. We identified CLN-5 and OCLN as targets of VEGF-A action in cortical and spinal cord endothelial cells and showed that both proteins, and BBB breakdown, were rescued in inflammatory and demyelinating plaques in the CNS of *GfapCre:Vegfa*$^{fl/fl}$ mice, in which VEGF-A inactivation was targeted to reactive astrocytes. We further identified the downstream effector eNOS as mediating the effects of VEGF-A on CLN-5 and the BBB. Finally, we showed that treatment with the selective eNOS inhibitor cavtratin during the acute clinical phase of EAE protected against paralysis and pathology, similar to the EAE phenotype seen in *GfapCre:Vegfa*$^{fl/fl}$ mice. Collectively, our findings suggested blockade of endothelial VEGF-A signaling as an avenue by which to restrict clinical severity and tissue damage in inflammatory CNS conditions (Figure 9).

Recent work has examined the role of pericytes in BBB maintenance (6–8), but earlier studies also define important astrocytic functions at the BBB (9, 10), and it was on the latter cell type that our work here focused. Astrocytes respond to CNS inflammation or injury with a graded spectrum of molecular expression, hypertrophy, and, in severe cases, scarring (45). These changes, called reactive astrogliosis, affect surrounding neural and non-neural cells beneficially or detrimentally, depending on the pathways driving the astroglial phenotype (34, 46, 47). Studies have identified astrocytes as regulators of BBB induction and maintenance (9–11) and have implicated astrogliosis, particularly induced by IL-1, as a driver of both BBB breakdown and repair (10, 12, 48). The mediators producing the effects of reactive astrocytes are incompletely characterized, and our data revealed VEGF-A as an important astrocyte-derived inducer of BBB disruption and pathology in vivo. Although VEGF-A–induced vascular permeability has previously been implicated in pathogenesis of disorders, including myocardial infarction, CNS hypoxia/reperfusion injury, and tumor growth and metastasis (49), and we and others have previously speculated on its role in BBB breakdown (12, 26), this study is the first to our knowledge to show the significance of astrocyte-derived VEGF-A in lesion pathogenesis and generation of clinical deficit in models of CNS inflammatory disease.

The BBB uses endothelial tight junctions to generate a physical barrier, allowing control of transcellular molecular trafficking via endothelial transporters and channels (1, 2). Disruption of the endothelial tight junction transmembrane proteins CLN-3, CLN-5, and OCLN correlates with BBB opening in EAE (4, 12), and downregulation of CLN-5 is linked to BBB breakdown in glioblastoma multiforme (50) and models of amyotrophic lateral sclerosis (51) and viral encephalomyelitis (52). Redistribution of CLN-5 and OCLN away from the cell membrane has also been implicated in BBB disruption in inflammatory models (53). Importantly, our data showed that VEGF-A downregulated endothelial expression of both CLN-5 and OCLN, and we observed rescue of both proteins, and BBB integrity, in CNS inflammation in *GfapCre:Vegfa*$^{fl/fl}$ mice. To quantify BBB breakdown, we measured extravasation of fibrinogen, albumin, and Ig. In the healthy CNS, these proteins are confined to the vasculature, and their leakage into the parenchyma has been widely used as an endogenous marker of BBB disruption (8, 11, 17). CNS entry of Igs and fibrinogen has also been linked to exacerbation of inflammation and demyelination and to inhibition of repair (17–19), suggesting relevance to lesion pathogenesis.

Our studies in vivo also showed that reduced BBB disruption in *GfapCre:Vegfa*$^{fl/fl}$ mice was accompanied by mitigation of lymphocyte infiltration and implicated BBB integrity as an important mechanism underlying this effect. Whereas BBB breakdown was restricted in AdIL-1–induced lesions in *GfapCre:Vegfa*$^{fl/fl}$ mice, we found that endothelial adhesion molecule and chemokine expression and CNS induction of MMPs were the same as in other genotypes. VCAM-1 and ICAM-1 (54), as well as CC and CXC chemokines (55), are important in driving inflammatory cell transmigration, whereas MMPs facilitate entry through the glia limitans and infiltration into the CNS parenchyma (56). Using the focal, directly induced AdIL-1 model in *GfapCre:Vegfa*$^{fl/fl}$ mice allowed us to selectively examine the effect of VEGF-A–induced BBB breakdown on lymphocyte entry while retaining these other important variables. Critically, we also found in these experiments and in EAE studies that inhibition of BBB breakdown and leukocyte infiltration in *GfapCre:Vegfa*$^{fl/fl}$ mice was associated with restriction of gray and white matter pathology and with reduced clinical paralysis. Thus, our data implicate inhibition of VEGF-A signaling as a protective avenue in patients with CNS inflammation.

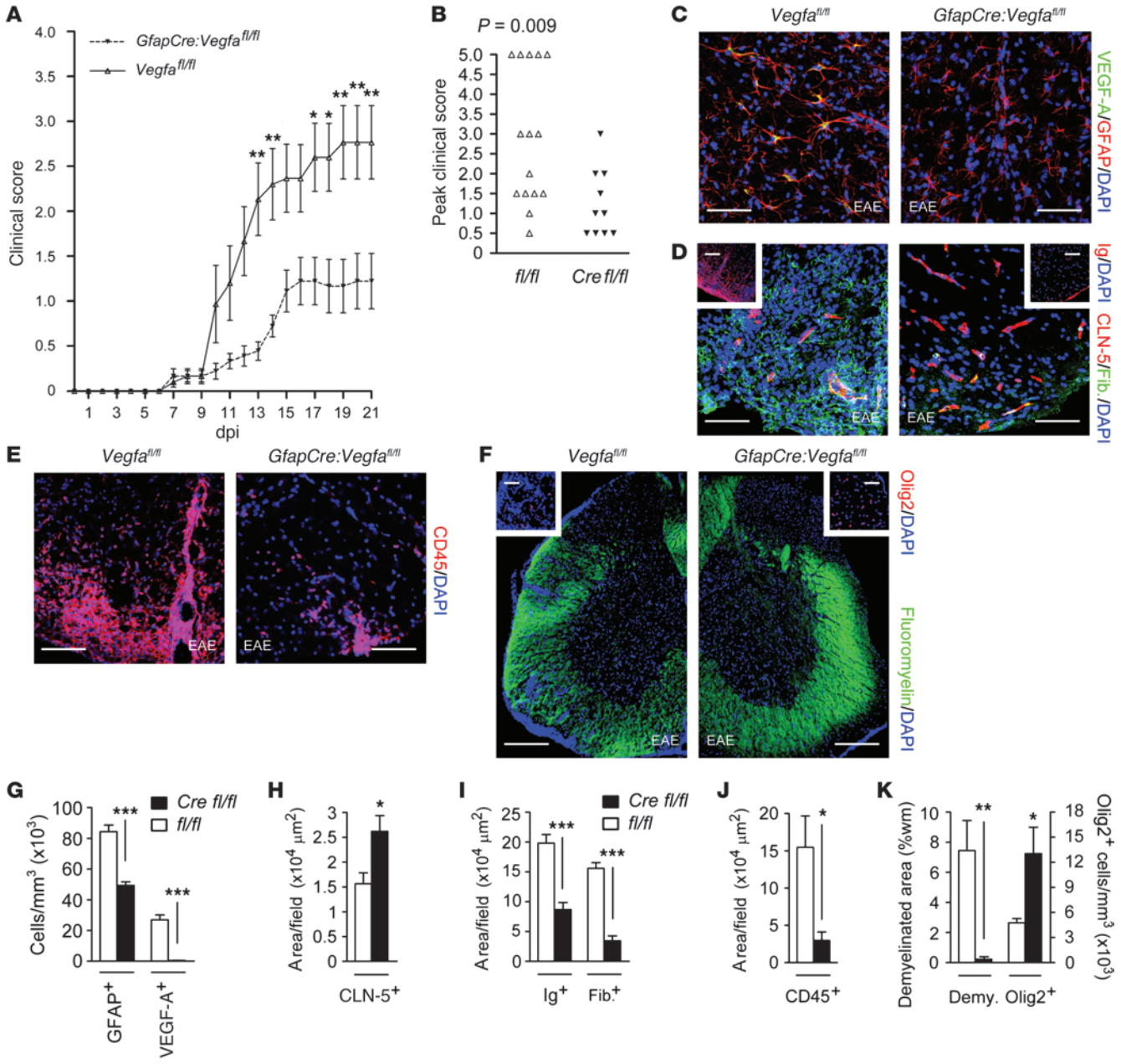

Figure 5

Restricted clinical deficit and tissue damage in EAE in *GfapCre:Vegfa*$^{fl/fl}$ mice. *GfapCre:Vegfa*$^{fl/fl}$ mice and *Vegfa*$^{fl/fl}$ littermates (8-week-old males, at least 10 per group) were sensitized with encephalitogenic $MOG_{35–55}$/CFA. (**A** and **B**) Disease was scored using a 5-point paradigm (35) and plotted (**A**) as a function of time and (**B**) by peak score. (**C**–**F**) EAE pathology, assessing for (**C**) astrogliosis, (**D**) BBB disruption, (**E**) inflammatory cell infiltration, and (**F**) demyelination and oligodendrocyte loss. (**G**–**K**) Respective morphometry of (**G**) VEGF-A and GFAP, as in **C**; (**H** and **I**) CLN-5, Ig, and fibrinogen, as in **D**; (**J**) CD45, as in **E**; and (**K**) Olig2 and demyelination (assessed by fluoromyelin), as in **F**. Scale bars: 50 μm (**C**–**E**); 150 μm (**F**); 40 μm (**D** and **F**, insets). **P* < 0.05, ***P* < 0.01, ****P* < 0.001, ANOVA plus Bonferroni test (**A**) or Student's *t* test (**B** and **G**–**K**). Data are representative of 3 independent experiments.

The transcription factor HIF-1α induces VEGF-A during development (36) and is induced transcriptionally by IL-1β in astrocytes, suggesting relevance to hypoxic/ischemic and inflammatory disease (23). However, although these data suggest HIF-1α as a potential route to inactivation of astrocytic VEGF-A, conditional *GfapCre:Hif1a*$^{fl/fl}$ mice displayed little effect on VEGF-A expression or BBB disruption in AdIL-1 lesions. These findings indicate that mechanisms regulating VEGF-A in embryogenesis and inflammation are likely distinct. However, our data do not invalidate roles in inflammatory lesion pathogenesis for other members of the family, for example, HIF-2α, which has previously been implicated as a regulator of astrocytic VEGF-A production in VHL-deficient mice and in oxygen-induced retinopathy (57). In addition, our findings focused on inflammation and did not address astrocytic responses to hypoxic/ischemic injury.

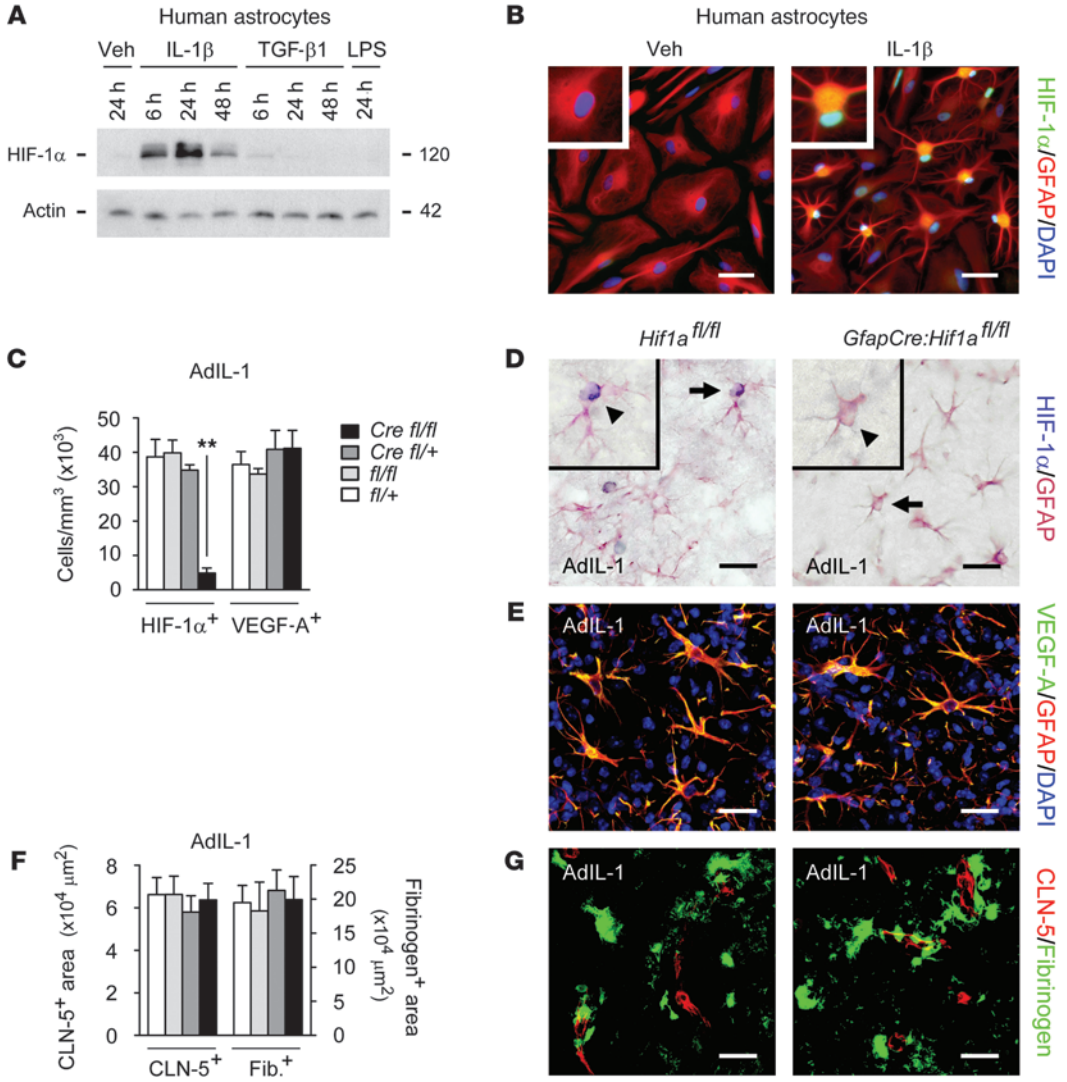

Figure 6

GfapCre:Hif1a$^{fl/fl}$ mice show normal VEGF-A expression and BBB opening in inflammatory lesions. (**A**) Primary human astrocytes were treated with 10 ng/ml IL-1β, TGF-β1, or LPS for the indicated times, and HIF-1α induction was examined by immunoblot. (**B**) Human astrocytes were treated with 10 ng/ml IL-1β or vehicle for 24 hours. In IL-1β–treated cultures, HIF-1α localized to astrocytic nuclei (inset; enlarged 2-fold). Results in **A** and **B** are typical of data from 3 separate cultures of human astrocytes from different brains. (**C**–**G**) AdIL-1 was microinjected into cortical gray matter of 12-week-old *GfapCre:Hif1a*$^{fl/fl}$ mice and littermate controls (n = 4 per genotype), and animals were sacrificed at 7 dpi. Immunostaining and morphometry were performed for (**C** and **D**) HIF-1α, (**C** and **E**) VEGF-A, and (**F** and **G**) fibrinogen (a measure of BBB breakdown) and CLN-5. In **D**, representative cells (arrows) are shown enlarged 2-fold in the insets (arrowheads). Results in **C**–**G** are representative of 3 independent experiments. Scale bars: 30 μm (**B**, **D**, and **E**); 40 μm (**G**). $^{**}P < 0.01$, ANOVA plus Bonferroni test.

The results of our analyses of endothelial VEGF-A signaling were more directly translational, identifying a therapeutic avenue by which to inhibit BBB breakdown. In CNS MVEC cultures, we found that VEGF-A downregulation of CLN-5 and OCLN occurred via VEGFR2 signaling through PLCγ and its effector, eNOS. Notably, targeting events within the endothelial cell allows for systemic delivery and avoids issues with CNS access, and our studies examining eNOS blockade in vivo validated this approach in a therapeutic setting. Tonic eNOS activity controls vascular tone and leukocyte trafficking in the resting state, whereas the activated form drives permeability and extravasation in disease (58). The phenotype of eNOS mutants combines inactivation of the tonic and activated forms and produces complex findings in EAE and carrageenan-induced inflammation (59). Understanding the translational potential of eNOS has been facilitated by development of selective inhibitors, notably cavtratin, a cell-permeable recombinant consisting of the eNOS-binding domain of caveolin-1 coupled to the homeodomain of *Drosophila* antennapedia (40–42). Cavtratin binds to eNOS via the caveolin-1 scaffolding domain, specifically inhibiting its enzymatic activity via protein-protein interaction (40, 42). Previous work has also shown that cavtratin does not block activity of other forms of NOS (40–42), and our experiments in vitro support these results (Figure 7F and Supplemental Figure 6E). Cavtratin reduces tumor microvascular permeability and progression (41)

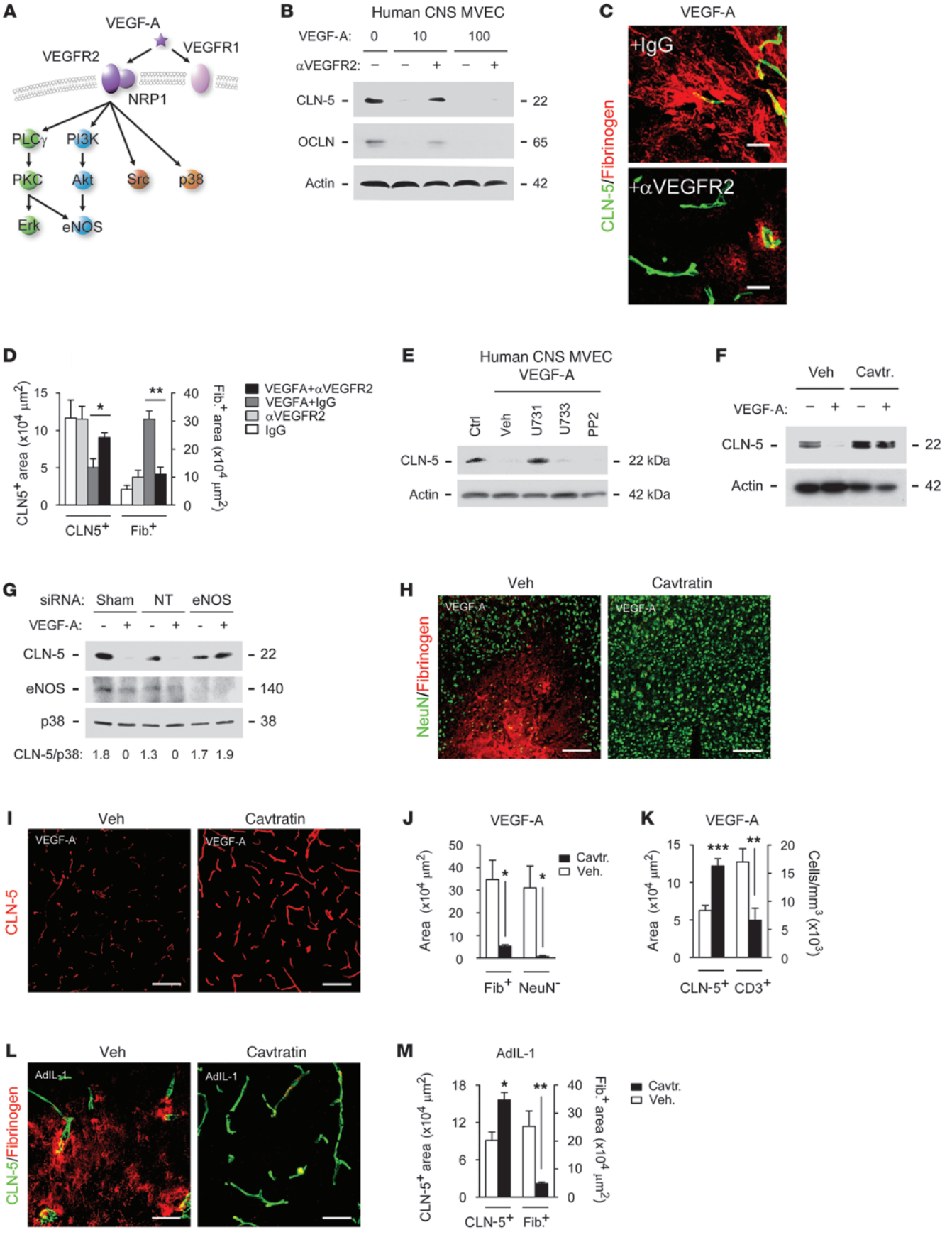
A
VEGF-A
VEGFR1
VEGFR2
NRP1
PLCγ
PI3K
PKC
Akt
Src
p38
Erk
eNOS
B
Human CNS MVEC
VEGF-A: 0 10 100
αVEGFR2: – – + – +
CLN-5
OCLN
Actin
22
65
42
C
VEGF-A
+IgG
+αVEGFR2
CLN-5/Fibrinogen
D
CLN5+ area (x10^4 μm^2)
Fib.+ area (x10^4 μm^2)
VEGFA+αVEGFR2
VEGFA+IgG
αVEGFR2
IgG
CLN5+
Fib.+
E
Human CNS MVEC
VEGF-A
Ctrl
Veh
U731
U733
PP2
CLN-5
Actin
22 kDa
42 kDa
F
Veh
Cavtr.
VEGF-A: – + – +
CLN-5
Actin
22
42
G
siRNA: Sham NT eNOS
VEGF-A: - + - + - +
CLN-5
eNOS
p38
22
140
38
CLN-5/p38: 1.8 0 1.3 0 1.7 1.9
H
Veh
Cavtratin
VEGF-A
NeuN/Fibrinogen
I
Veh
Cavtratin
VEGF-A
CLN-5
J
VEGF-A
Area (x10^4 μm^2)
Cavtr.
Veh.
Fib+
NeuN-
K
VEGF-A
Area (x10^4 μm^2)
Cells/mm^3 (x10^3)
CLN-5+
CD3+
L
Veh
Cavtratin
AdIL-1
CLN-5/Fibrinogen
M
AdIL-1
CLN-5+ area (x10^4 μm^2)
Fib.+ area (x10^4 μm^2)
Cavtr.
Veh.
CLN-5+
Fib.+

Figure 7
Effects of VEGF-A on CLN-5 are mediated via eNOS. (**A**) VEGF-A signaling pathways. (**B**) Human CNS MVECs were pretreated with 10 ng/ml anti-VEGFR2 or IgG for 2 hours, then VEGF-A or vehicle for 24 hours, and CLN-5 and OCLN levels were determined by immunoblot. (**C** and **D**) 12-week-old C57BL/6 mice (3 per group) received cortical coinjection of 20 ng VEGF-A or vehicle, plus 2 μg anti-VEGFR2 or IgG, and were sacrificed at 24 hours for determination of CLN-5 and fibrinogen area. (**E** and **F**) Immunoblot for CLN-5 in VEGF-A–treated human CNS MVECs also (**E**) treated with 5 μM U73122, 10 ng/ml VEGF-A, 5 μM U73343, or 3 μM PP2 or (**F**) pretreated with 2 μM cavtratin. (**G**) Immunoblot for CLN-5, eNOS, and p38 (representative of other signaling components) in human MVECs nucleofected with sham, nontargeting (NT), or eNOS siRNA. CLN-5/p38 ratio is shown below. (**H**–**M**) 12-week-old C57BL/6 mice (3 per group) received 2.5 mg/kg cavtratin or vehicle i.p., then 30 minutes later received cortical injection of (**H**–**K**) 60 ng VEGF-A, followed by sacrifice at 24 hours, or (**L** and **M**) 10^7 pfu AdIL-1, followed by daily cavtratin until sacrifice at 7 dpi. Immunostaining and morphometry for NeuN, fibrinogen, CLN-5, and CD3 are shown. Scale bars: 20 μm (**C**); 150 μm (**H**, **I**, and **L**). $^*P < 0.05$, $^{**}P < 0.01$, $^{***}P < 0.001$, ANOVA plus Bonferroni test (**D**) or Student's *t* test (**J**, **K**, and **M**). Results are representative of at least 3 separate cultures (**B** and **E**–**G**) or 3 independent experiments (**C**, **D**, and **H**–**M**).

and restricts edema in inflammatory models without influencing systemic hemodynamics (40). In CNS MVECs, our results showed that cavtratin matched the effect of eNOS siRNA in abrogating VEGF-A–induced downregulation of CLN-5 and OCLN, and its administration in vivo produced a phenotype similar to that seen in *GfapCre:Vegfa*$^{fl/fl}$ mice in terms of blockade of BBB breakdown, lymphocyte infiltration, and tissue damage in inflammatory lesions. Importantly, treatment in the acute stages of EAE was also protective, suggestive of relevance to human disease.

These data suggest further studies to investigate roles of VEGF-A and eNOS in other inflammatory CNS conditions. For example, blocking the pathway might be effective in preventing CNS entry of extrathecally produced autoantibodies in diseases such as neuromyelitis optica. These approaches may also represent a means by which to examine the role of BBB permeability in disorders characterized by slowly accumulating tissue damage accompanied by low-grade inflammation and BBB leakage, such as primary or secondary progressive MS (16). It might also be interesting to combine inhibition of inducers of BBB disruption, such as VEGF-A–eNOS and MMPs, with activation of pathways promoting barrier formation and/or repair, such as Shh signaling (11), for potentially additive or synergistic outcomes.

Methods

Cytokines and growth factors. Human IL-1β, P*l*GF, and VEGF-C and mouse $VEGF_{165}$ and $VEGF_{121}$ were from Peprotech. Human VEGF-A, IFN-γ, TGF-β1, and IL-6 were from R&D Systems. Human and mouse VEGF-A were used at 1–100 ng/ml, human $VEGF_{165}$ and $VEGF_{121}$ at 1–20 ng/ml, and other factors at 10 ng/ml.

Expression constructs. The adenoviral IL-1β vector AdIL1 and control AdDL70 were gifts from J. Gauldie (McMaster University, Hamilton, Ontario, Canada; ref. 30). Previous work has shown that intracerebral microinjection of 10^7 pfu AdIL1, but not empty vector, induces inflammation, astro- and microgliosis, and BBB breakdown at 8–14 dpi (31).

Antibodies. Anti–CLN-5 (mouse), anti-OCLN, anti-cingulin, anti–ZO-1 (rabbit), anti-GFAP (rat), and anti-fluoromyelin were from Invitrogen. Anti–VEGF-A (rabbit) was from Santa Cruz Biotech. Anti-albumin (sheep) and anti-CD3 were from Abcam. Anti-fibrinogen (rabbit) and anti-FVIIIR (mouse) were from Dako. Antibodies for phosphorylated versus total eNOS, p44/42, p-GSK3, PLCγ, and Src and for cleaved caspase-3 (rabbit) were from Cell Signaling. Mouse anti-eNOS was from BD. Anti-CD4, anti-CD19, anti-CXCL10, anti-CXCL12, anti-VEGFR2, anti–VCAM-1, and anti–ICAM-1 (rat or rabbit) were from eBioscience. Anti–HIF-1α was from ThermoScientific. Antibodies for NeuN and Olig2 were from Millipore, and Sternberger mouse anti-MBP was from Covance.

Inhibitors. Anti-VEGFR2 blocking antibody and control IgG (10 ng/ml) were from R&D Systems. The PLCγ1 inhibitor U73122 and inactive analog U73343 (both 5 μM), Src kinase inhibitor PP2 (3 μM), eNOS inhibitor cavtratin (2 μM in vitro, 2.5 mg/kg in vivo) (40), NOS inhibitors L-NIO and L-NAME (both 100 μM) (43), and DPI (50 μM) were from EMD. The p44/42 inhibitor U0126 (10 μM) and PI3K inhibitor LY294002 (20 μM) were from Cell Signaling. Efficacy and specificity were confirmed by blotting with phosphospecific antibodies (Supplemental Figure 6), and toxicity was monitored using TUNEL and LDH assays (Promega). Human CNS MVEC cultures were transferred into medium with inhibitor, homolog, or vehicle for 2 hours, then VEGF-A was added and protein harvested 1–24 hours later.

Mice. *GfapCre* mice (generated in the M.V. Sofroniew lab) express Cre recombinase under a 15-kb promoter cassette containing the murine *Gfap* gene and all introns and regulatory elements (28). Cre expression is astrocyte specific except in areas of adult neurogenesis, where it is also observed in some neural progenitors (28). *Vegfa*^{fl} mice were generated in the N. Ferrara lab and have been reported previously (29). *Hif1a*^{fl} mice were made in the laboratory of R. Johnson (UCSD, San Diego, California, USA; ref. 37) and purchased from Jackson Laboratories. All lines were backcrossed onto the C57BL/6 background for more than 10 generations. For most experiments, *GfapCre:Vegfa*$^{+/fl}$ mice were crossed with *Vegfa*$^{fl/fl}$ animals to generate *GfapCre:Vegfa*$^{fl/fl}$ mice and controls, and a similar strategy was used to generate *GfapCre:Hif1a*$^{fl/fl}$ mice. To generate larger numbers of mice for EAE studies, *GfapCre:Vegfa*$^{fl/fl}$ animals were crossed with *Vegfa*$^{fl/fl}$ mice. Genotyping primers were as follows: *GfapCre* (forward, ACCAGCCAGCTATCAACTC; reverse, TATACGCGTGCTAGCGAAGATCTCCATCTTCCAGCAG; band, 350 bp); *Vegfa*^{fl} (forward, CCTGGCCCTCAAGTACACCTT; reverse, TCCGTACGACGCATTTCTAG; band, 108 and 148 bp for WT and flox, respectively); *Hif1a*^{fl} (forward, TGCTCATCAGTTGCCACTT; reverse, GTTGGGGCAGTACTGGAAAG; band, 650 and 700 bp for WT and flox, respectively). PCR conditions were as follows: 94°C for 4 minutes; 35 cycles of 94°C for 30 seconds, 56°C for 30 seconds, and 72°C for 30 seconds; then 72°C for 10 minutes. C57BL/6 mice were from Jackson.

Stereotactic microinjection. Mice (12 weeks of age, 4 per genotype per condition per time point, unless otherwise indicated) were anesthetized and placed into a stereotactic frame (Kopf Instruments). For injection of AdIL1 or AdDL70 control (10^7 pfu) or mouse $VEGF_{164}$ (60 ng, in 3 μl of PBS/BSA vehicle) or vehicle into layers IV and V of cortical gray matter, coordinates used were *y* of 1 mm caudal to Bregma, *x* of 2 mm (left), and *z* of 1.5 mm (12). For induction of focal demyelination in corpus callosum, 1.5 μl 1% lysolecithin was delivered at *y* of 5.5 mm anterior to Lambda, *x* of 1 mm (left), and *z* of 2 mm (33). Mice were harvested by perfusion with 4% paraformaldehyde at 24 hours to 14 dpi.

EAE. Mice (8-week-old males on the C57BL/6 background, at least 10 per group) were immunized s.c. with 300 μg $MOG_{35–55}$ (Invitrogen) in 200 μl CFA containing 300 μg/ml *Mycobacterium tuberculosis* H37Ra (Difco) in the dorsum. Mice received 500 ng pertussis toxin i.p. at 0 and 2 dpi. Disease was scored as follows: 0, no symptoms; 1, floppy tail; 2, hindlimb weakness; 3, hindlimb paralysis; 4, fore- and hindlimb paralysis; 5, death (35).

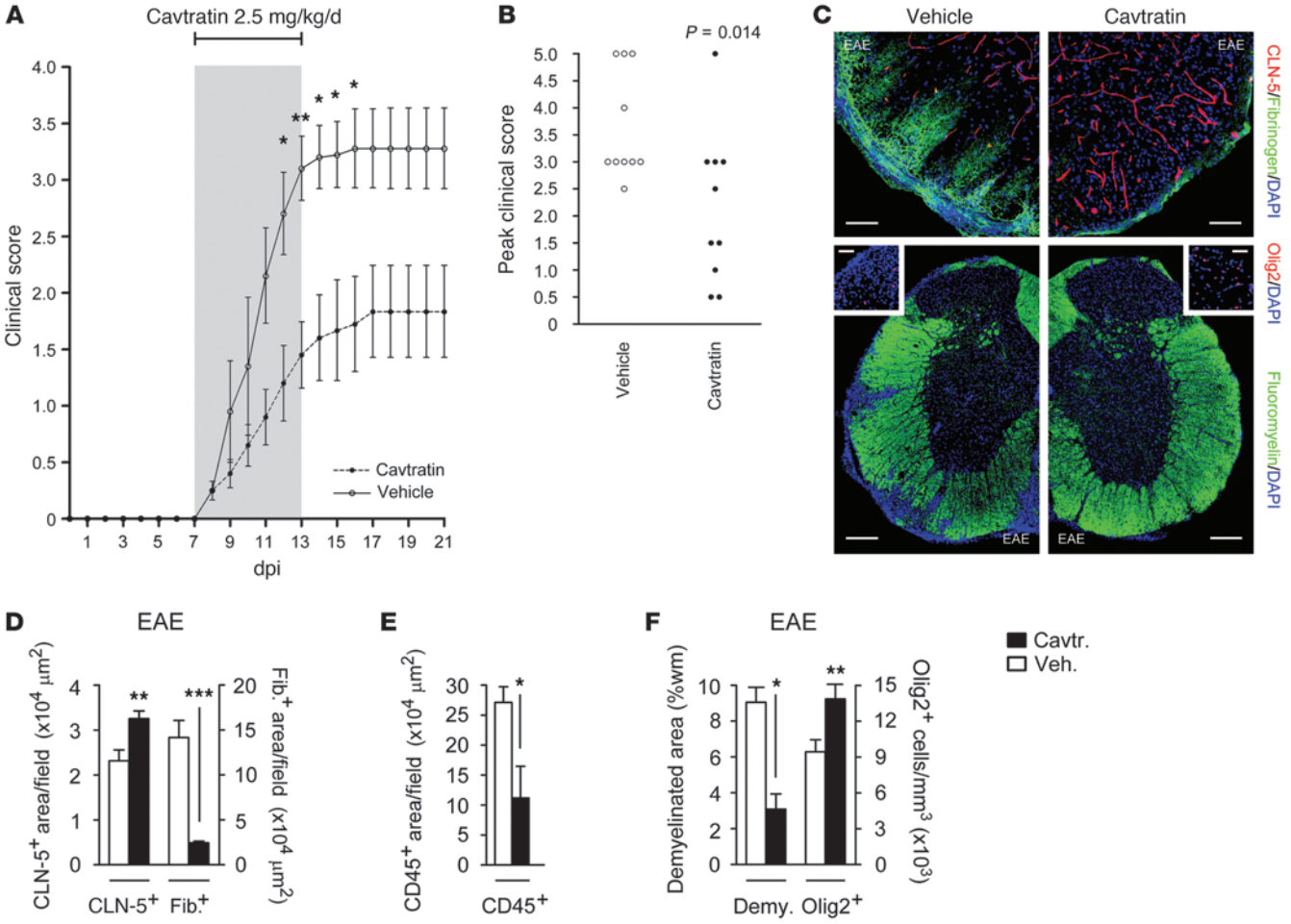

Figure 8

Reduced clinical severity and neuropathology of EAE in cavtratin-treated mice. Mice (8-week-old male C57BL/6, 10 per group) were sensitized with $MOG_{35–55}$/CFA, then from onset of weight loss (7 dpi) treated for 7 days with 2.5 mg/kg/d i.p. cavtratin or vehicle. (**A** and **B**) Disease was scored using a 5-point paradigm (35) and plotted (**A**) as a function of time and (**B**) by peak score. (**C**) Lumbar spinal cord sections were subjected to immunostaining at 21 dpi to assess BBB breakdown (top) as well as demyelination and oligodendrocyte loss (bottom). (**D**–**F**) Morphometry of (**D**) fibrinogen (a measure of BBB breakdown) and CLN-5, (**E**) CD45 (a measure of inflammatory cell infiltration), and (**F**) Olig2 and demyelination (assessed by fluoromyelin). These findings resembled the phenotype of EAE in *GfapCre:Vegfa$^{fl/fl}$* mice (see Figure 5). Scale bars: 50 μm (**C**, top); 150 μm (**C**, bottom); 40 μm (**C**, insets). $^*P < 0.05$, $^{**}P < 0.01$, $^{***}P < 0.001$, ANOVA plus Bonferroni test (**A**) or Student's *t* test (**B** and **D**–**F**). Data are representative of 3 independent experiments.

Immunohistochemistry. Embedding and immunostaining were as previously described (12) unless otherwise indicated. For claudins, prior to blocking, sections were soaked in EDTA (pH 8; 100°C). For OCLN, VEGF-A, CXCL12, CD4, and CD19, sections were treated with 0.5 mg/ml protease XIV (Sigma-Aldrich) at 37°C for 5 minutes. For VEGFR2, sections were treated with 1% SDS for 5 minutes at room temperature. Primary antibodies were used at 1:100 except CLN-5 (1:50), fibrinogen (1:1,000), and albumin (1:1,000). Fluoromyelin was used at 1:200 in final wash. Samples were examined using a Leica Microsystems confocal microscope, and stacks were collected with *z* of 1 μm.

Morphometric analysis. Morphometric analyses were carried out using NIH ImageJ software. Pixels positive for CD11b, CLN-5, OCLN, fibrinogen, albumin, VCAM-1, ICAM-1, CXCL10, and CXCL12 immunoreactivity, or cells positive for CD4, CD19, GFAP, VEGF-A, HIF-1α, or Olig2 were counted by a blinded observer in projections from cortical sections with the same number of images from at least 4 animals per condition per genotype per time point and 4 age- and sex-matched normal controls (unless otherwise indicated): at least 5 random ×20 fields in 5 sections per animal. Neuronal and myelin loss were quantified using previously published analyses (35); $NeuN^-$ or MBP^- pixels were subtracted from the total in each field in matched projections at ×20 magnification using ImageJ software, and data were converted to absolute area.

Cell culture. Primary human fetal astrocyte cultures were established from 3 different brains, as described previously (23). Primary human CNS MVECs were purchased from Cell Systems Inc. and cultured in complete serum-containing medium. Primary mouse cortical MVECs and spinal cord MVEC cultures were established as described previously (12).

siRNA. Human MVEC cultures were nucleofected with siRNA for eNOS or other components of VEGF-A signaling, with nontargeting control siRNA, or with transfection reagent alone (sham) using Amaxa nucleofector program T05 (Amaxa), then treated with VEGF-A. At 24 hours, protein extracts were harvested and subjected to immunoblotting

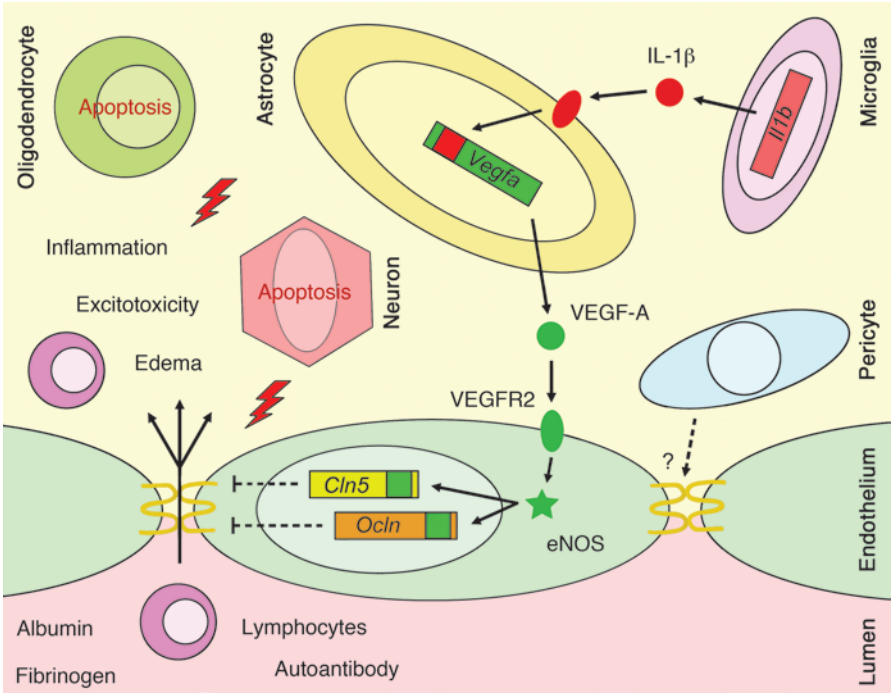

Figure 9
Proposed mechanism underlying BBB disruption in CNS inflammatory lesions. The inflammatory cytokine IL-1β is produced early in lesion pathogenesis by mononuclear phagocytes and binds to its receptor on astrocytes adjacent to CNS microvessels, leading to *Vegfa* induction. VEGF-A released from the astrocyte binds to VEGFR2 on CNS MVECs, activating eNOS-dependent downregulation of *Cln5* and *Ocln* and leading to disruption of endothelial tight junctions and BBB breakdown. These events facilitate parenchymal entry of autoantibodies, plasma proteins, and lymphocytes, leading to inflammation, edema, and excitotoxicity and exacerbation of neuropathology. How these astrocyte-driven effects interact with pericyte effects at the BBB is not known.

for CLN-5 and targeted and nontargeted control signaling molecules to confirm siRNA efficacy and specificity.

Immunoblotting. SDS-PAGE and blotting were carried out as reported previously (23). Nonsaturated films were scanned using a Canon LiDE scanner, band pixel density was measured using ImageJ software and standardized to loading control, and fold change was calculated.

Immunocytochemistry. Cultures were fixed and stained as described previously (12). For claudins, cells were fixed in 95% ethanol at 4°C for 30 minutes, then in 1:1 methanol/acetone for 1 minute at room temperature. Primary antibodies were used at 1:100, except CLN-5 (1:50). Cultures were examined as described above, and stacks were collected with *z* of 0.5 μm.

ELISA. Multiplex ELISA kits for human CXCL1, CXCL8, CXCL10, CCL2, IL-6, TNF-α, and VEGF-A were from Millipore and R&D Systems.

Statistics. Data represent mean ± SEM. For multiple comparisons, 1-way ANOVA plus Bonferroni post-test was used. 2-tailed Student's *t* test was used to compare 2 groups of matched samples. A *P* value less than 0.05 was considered significant.

Study approval. Animal studies were approved by the MSSM Institutional Animal Care and Use Committee. Experiments in human cell cultures were approved by the MSSM Institutional Review Board. As verified by the MSSM Institutional Review Board and in line with local, state, and federal regulations, informed consent was not required for the use of cell cultures in the present study; the cultures have exempt status since they are prepared from postmortem deidentified tissue samples.

Acknowledgments

The authors thank Victor Friedrich and Rumana Huq of the MSSM Microscopy Shared Resource Facility for assistance with imaging. We thank Celia Brosnan, Tara Desilva, Carmen Melendez-Vasquez, and Cedric Raine for advice regarding the manuscript. This work was supported by United States Public Health Service grants R01NS046620, R01NS062703, R01NS056074, and ARRA R01NS056074-02S1 (to G.R. John) and R01NS057624 (to M.V. Sofroniew). Support for A.T. Argaw was from United States Public Health Service grant T32NS051147-03. Support for J. Seto was from United States Public Health Service contract HHSN272201000054C. This study was also supported by National MS Society Research Grants RG3874 and RG4127 (to G.R. John) and the Jayne and Harvey Beker Foundation and Noto Foundation (to G.R. John). The MSSM Analytical Imaging Facility is supported by NIH/NCI grant R24CA095823.

Received for publication September 6, 2011, and accepted in revised form April 18, 2012.

Address correspondence to: Gareth R. John, Department of Neurology, Annenberg 14-86, Mount Sinai School of Medicine, 1 Gustave L. Levy Place, New York, New York 10029-6574, USA. Phone: 212.241.8142; Fax: 212.348.1310; E-mail: gareth.john@mssm.edu.

1. Zlokovic BV. The blood-brain barrier in health and chronic neurodegenerative disorders. *Neuron*. 2008;57(2):178–201.
2. Hawkins BT, Davis TP. The blood-brain barrier/neurovascular unit in health and disease. *Pharmacol Rev*. 2005;57(2):173–185.
3. Nitta T, et al. Size-selective loosening of the blood-brain barrier in claudin-5-deficient mice. *J Cell Biol*. 2003;161(3):653–660.
4. Wolburg H, et al. Localization of claudin-3 in tight junctions of the blood-brain barrier is selectively lost during experimental autoimmune encephalomyelitis and human glioblastoma multiforme. *Acta Neuropathol*. 2003;105(6):586–592.
5. Saitou M, et al. Occludin-deficient embryonic stem cells can differentiate into polarized epithelial cells bearing tight junctions. *J Cell Biol*. 1998;141(2):397–408.
6. Daneman R, Zhou L, Kebede AA, Barres BA. Pericytes are required for blood-brain barrier integrity during embryogenesis. *Nature*. 2010;468(7323):562–566.
7. Armulik A, et al. Pericytes regulate the blood-brain barrier. *Nature*. 2010;468(7323):557–561.
8. Bell RD, et al. Pericytes control key neurovascular functions and neuronal phenotype in the adult brain and during brain aging. *Neuron*. 2010;68(3):409–427.
9. Hayashi Y, Nomura M, Yamagishi S, Harada S, Yamashita J, Yamamoto H. Induction of various blood-brain barrier properties in non-neural endothelial cells by close apposition to co-cultured astrocytes. *Glia*. 1997;19(1):13–26.
10. Bush TG, et al. Leukocyte infiltration, neuronal degeneration, and neurite outgrowth after ablation of scar-forming, reactive astrocytes in adult

transgenic mice. *Neuron*. 1999;23(2):297–308.
11. Alvarez JI, et al. The Hedgehog pathway promotes blood-brain barrier integrity and CNS immune quiescence. *Science*. 2011;334(6063):1727–1731.
12. Argaw AT, Gurfein BT, Zhang Y, Zameer A, John GR. VEGF-mediated disruption of endothelial CLN-5 promotes blood-brain barrier breakdown. *Proc Natl Acad Sci U S A*. 2009;106(6):1977–1982.
13. Bruck W, Bitsch A, Kolenda H, Bruck Y, Stiefel M, Lassmann H. Inflammatory central nervous system demyelination: correlation of magnetic resonance imaging findings with lesion pathology. *Ann Neurol*. 1997;42(5):783–793.
14. Dallasta LM, et al. Blood-brain barrier tight junction disruption in human immunodeficiency virus-1 encephalitis. *Am J Pathol*. 1999;155(6):1915–1927.
15. Sandoval KE, Witt KA. Blood-brain barrier tight junction permeability and ischemic stroke. *Neurobiol Dis*. 2008;32(2):200–219.
16. Miller DH, Grossman RI, Reingold SC, McFarland HF. The role of magnetic resonance techniques in understanding and managing multiple sclerosis. *Brain*. 1998;121(pt 1):3–24.
17. Adams RA, et al. The fibrin-derived gamma377-395 peptide inhibits microglia activation and suppresses relapsing paralysis in central nervous system autoimmune disease. *J Exp Med*. 2007;204(3):571–582.
18. Schluesener HJ, Sobel RA, Linington C, Weiner HL. A monoclonal antibody against a myelin oligodendrocyte glycoprotein induces relapses and demyelination in central nervous system autoimmune disease. *J Immunol*. 1987;139(12):4016–4021.
19. Schachtrup C, et al. Fibrinogen inhibits neurite outgrowth via beta 3 integrin-mediated phosphorylation of the EGF receptor. *Proc Natl Acad Sci U S A*. 2007;104(28):11814–11819.
20. Germano A, et al. NMDA receptor antagonist felbamate reduces behavioral deficits and blood-brain barrier permeability changes after experimental subarachnoid hemorrhage in the rat. *J Neurotrauma*. 2007;24(4):732–744.
21. Graesser D, et al. Altered vascular permeability and early onset of experimental autoimmune encephalomyelitis in PECAM-1-deficient mice. *J Clin Invest*. 2002;109(3):383–392.
22. DeAngelis T, Lublin F. Multiple sclerosis: new treatment trials and emerging therapeutic targets. *Curr Opin Neurol*. 2008;21(3):261–271.
23. Argaw AT, et al. IL-1beta regulates blood-brain barrier permeability via reactivation of the hypoxia-angiogenesis program. *J Immunol*. 2006; 177(8):5574–5584.
24. Ferrara N, et al. Heterozygous embryonic lethality induced by targeted inactivation of the *Vegf* gene. *Nature*. 1996;380(6573):439–442.
25. Carmeliet P, et al. Abnormal blood vessel development and lethality in embryos lacking a single *Vegf* allele. *Nature*. 1996;380(6573):435–439.
26. Dobrogowska DH, Lossinsky AS, Tarnawski M, Vorbrodt AW. Increased blood-brain barrier permeability and endothelial abnormalities induced by vascular endothelial growth factor. *J Neurocytol*. 1998;27(3):163–173.
27. Proescholdt MA, Jacobson S, Tresser N, Oldfield EH, Merrill MJ. Vascular endothelial growth factor is expressed in multiple sclerosis plaques and can induce inflammatory lesions in experimental allergic encephalomyelitis rats. *J Neuropathol Exp Neurol*. 2002;61(10):914–925.
28. Garcia AD, Doan NB, Imura T, Bush TG, Sofroniew MV. GFAP-expressing progenitors are the principal source of constitutive neurogenesis in adult mouse forebrain. *Nat Neurosci*. 2004;7(11):1233–1241.
29. Gerber HP, et al. VEGF is required for growth and survival in neonatal mice. *Development*. 1999; 126(6):1149–1159.
30. Margetts PJ, et al. Inflammatory cytokines, angiogenesis, and fibrosis in the rat peritoneum. *Am J Pathol*. 2002;160(6):2285–2294.
31. Ferrari CC, et al. Reversible demyelination, blood-brain barrier breakdown, and pronounced neutrophil recruitment induced by chronic IL-1 expression in the brain. *Am J Pathol*. 2004;165(5):1827–1837.
32. Martinelli V, et al. A short-term randomized MRI study of high-dose oral vs intravenous methylprednisolone in MS. *Neurology*. 2009;73(22):1842–1848.
33. Zhang J, et al. Proapoptotic and antiapoptotic actions of Stat1 versus Stat3 underlie neuroprotective and immunoregulatory functions of IL-11. *J Immunol*. 2011;187(3):1129–1141.
34. Choi JW, et al. FTY720 (fingolimod) efficacy in an animal model of multiple sclerosis requires astrocyte sphingosine 1-phosphate receptor 1 (S1P1) modulation. *Proc Natl Acad Sci U S A*. 2011;108(2):751–756.
35. Gurfein BT, et al. IL-11 regulates autoimmune demyelination. *J Immunol*. 2009;183(7):4229–4240.
36. Forsythe JA, et al. Activation of vascular endothelial growth factor gene transcription by hypoxia-inducible factor 1. *Mol Cell Biol*. 1996;16(9):4604–4613.
37. Higgins DF, et al. Hypoxia promotes fibrogenesis in vivo via HIF-1 stimulation of epithelial-to-mesenchymal transition. *J Clin Invest*. 2007;117(12):3810–3820.
38. Robinson CJ, Stringer SE. The splice variants of vascular endothelial growth factor (VEGF) and their receptors. *J Cell Sci*. 2001;114(pt 5):853–865.
39. Olsson AK, Dimberg A, Kreuger J, Claesson-Welsh L. VEGF receptor signalling - in control of vascular function. *Nat Rev Mol Cell Biol*. 2006;7(5):359–371.
40. Bucci M, et al. In vivo delivery of the caveolin-1 scaffolding domain inhibits nitric oxide synthesis and reduces inflammation. *Nat Med*. 2000; 6(12):1362–1367.
41. Gratton JP, et al. Selective inhibition of tumor microvascular permeability by cavtratin blocks tumor progression in mice. *Cancer Cell*. 2003; 4(1):31–39.
42. Bernatchez PN, Bauer PM, Yu J, Prendergast JS, He P, Sessa WC. Dissecting the molecular control of endothelial NO synthase by caveolin-1 using cell-permeable peptides. *Proc Natl Acad Sci U S A*. 2005;102(3):761–766.
43. Rees DD, Palmer RM, Schulz R, Hodson HF, Moncada S. Characterization of three inhibitors of endothelial nitric oxide synthase in vitro and in vivo. *Br J Pharmacol*. 1990;101(3):746–752.
44. Zhao W, et al. Experimental allergic encephalomyelitis in the rat is inhibited by aminoguanidine, an inhibitor of nitric oxide synthase. *J Neuroimmunol*. 1996;64(2):123–133.
45. Sofroniew MV. Molecular dissection of reactive astrogliosis and glial scar formation. *Trends Neurosci*. 2009;32(12):638–647.
46. Raasch J, et al. IkappaB kinase 2 determines oligodendrocyte loss by non-cell-autonomous activation of NF-kappaB in the central nervous system. *Brain*. 2011;134(pt 4):1184–1198.
47. Kang Z, et al. Astrocyte-restricted ablation of interleukin-17-induced Act1-mediated signaling ameliorates autoimmune encephalomyelitis. *Immunity*. 2010;32(3):414–425.
48. Herx LM, Yong VW. Interleukin-1 beta is required for the early evolution of reactive astrogliosis following CNS lesion. *J Neuropathol Exp Neurol*. 2001;60(10):961–971.
49. Weis SM, Cheresh DA. Pathophysiological consequences of VEGF-induced vascular permeability. *Nature*. 2005;437(7058):497–504.
50. Liebner S, et al. Claudin-1 and claudin-5 expression and tight junction morphology are altered in blood vessels of human glioblastoma multiforme. *Acta Neuropathol*. 2000;100(3):323–331.
51. Zhong Z, et al. ALS-causing SOD1 mutants generate vascular changes prior to motor neuron degeneration. *Nat Neurosci*. 2008;11(4):420–422.
52. Gralinski LE, Ashley SL, Dixon SD, Spindler KR. Mouse adenovirus type 1-induced breakdown of the blood-brain barrier. *J Virol*. 2009;83(18):9398–9410.
53. Stamatovic SM, Keep RF, Kunkel SL, Andjelkovic AV. Potential role of MCP-1 in endothelial cell tight junction 'opening': signaling via Rho and Rho kinase. *J Cell Sci*. 2003;116(pt 22):4615–4628.
54. Yednock TA, Cannon C, Fritz LC, Sanchez-Madrid F, Steinman L, Karin N. Prevention of experimental autoimmune encephalomyelitis by antibodies against alpha 4 beta 1 integrin. *Nature*. 1992;356(6364):63–66.
55. McCandless EE, Wang Q, Woerner BM, Harper JM, Klein RS. CXCL12 limits inflammation by localizing mononuclear infiltrates to the perivascular space during experimental autoimmune encephalomyelitis. *J Immunol*. 2006;177(11):8053–8064.
56. Yong VW. Metalloproteinases: mediators of pathology and regeneration in the CNS. *Nat Rev Neurosci*. 2005;6(12):931–944.
57. Weidemann A, et al. Astrocyte hypoxic response is essential for pathological but not developmental angiogenesis of the retina. *Glia*. 2010; 58(10):1177–1185.
58. Cirino G, Fiorucci S, Sessa WC. Endothelial nitric oxide synthase: the Cinderella of inflammation? *Trends Pharmacol Sci*. 2003;24(2):91–95.
59. Wu M, Tsirka SE. Endothelial NOS-deficient mice reveal dual roles for nitric oxide during experimental autoimmune encephalomyelitis. *Glia*. 2009;57(11):1204–1215.